



# Spectroscopic optical coherence tomography: A review of concepts and biomedical applications

Hyeong Soo Nam and Hongki Yoo

Department of Biomedical Engineering, Hanyang University, Seoul, Republic of Korea

## ABSTRACT

Optical coherence tomography (OCT) is a 3-dimensional high-resolution imaging modality based on an interferometry and is widely used in a large variety of medical fields. Spectroscopic OCT (S-OCT) is a signal-processing method that uses the raw interferograms generated by OCT to investigate depth-resolved spectroscopic profiles of a sample. The spectroscopic information provided by S-OCT can be used to enhance the contrast of OCT images and overcome the limitations of gray-scale OCT images that describe only morphology. In this review, we present the concepts behind S-OCT as well as acquisition methods and description of obtainable spectroscopic properties. Furthermore, this review covers the biomedical applications of the spectroscopic information that can be obtained with S-OCT, including measurements of hemoglobin concentrations, blood oxygen saturation levels, atherosclerotic plaque detection, evaluation of burn injuries, contrast enhancement using exogenous contrast agents, and detection of precancerous lesions.

## KEYWORDS

Spectroscopy; spectroscopic optical coherence tomography; optical coherence tomography

## Introduction

Optical coherence tomography (OCT) (1) is a non-invasive 3-dimensional imaging technique based on interferometry that provides depth-resolved tomographic images of a sample. The high resolution of OCT ( $\sim 10 \mu\text{m}$ ) (2) permits visualization of the microscopic structure of samples. Moreover, OCT operates at a much faster speed than other tomography devices (e.g., ultrasound) because it is based on light. Especially, Fourier-domain OCT (FD-OCT) (3, 4) is advantageous with respect to both operation speed and sensitivity compared to time-domain OCT (5) and can be used for *in vivo* real-time imaging of biological tissue. The light source for FD-OCT is based on either a broadband light source or frequency-swept light source with a wide bandwidth of  $>100 \text{ nm}$  (2). Light from the light source is divided into a sample arm and a reference arm (Figure 1). The reflected light from the reference arm and the back-scattered light from the sample arm interfere with each other, generating an interferogram in which depth information is encoded as frequency. The depth information can be reconstructed by subjecting the interferogram to

**CONTACT** Hongki Yoo ✉ [hyoo@hanyang.ac.kr](mailto:hyoo@hanyang.ac.kr) 📠 Department of Biomedical Engineering, Hanyang University, Seoul 04763, Republic of Korea.

Color versions of one or more figures in this article are available online at [www.tandfonline.com/laps](http://www.tandfonline.com/laps).

© 2018 Taylor & Francis Group, LLC

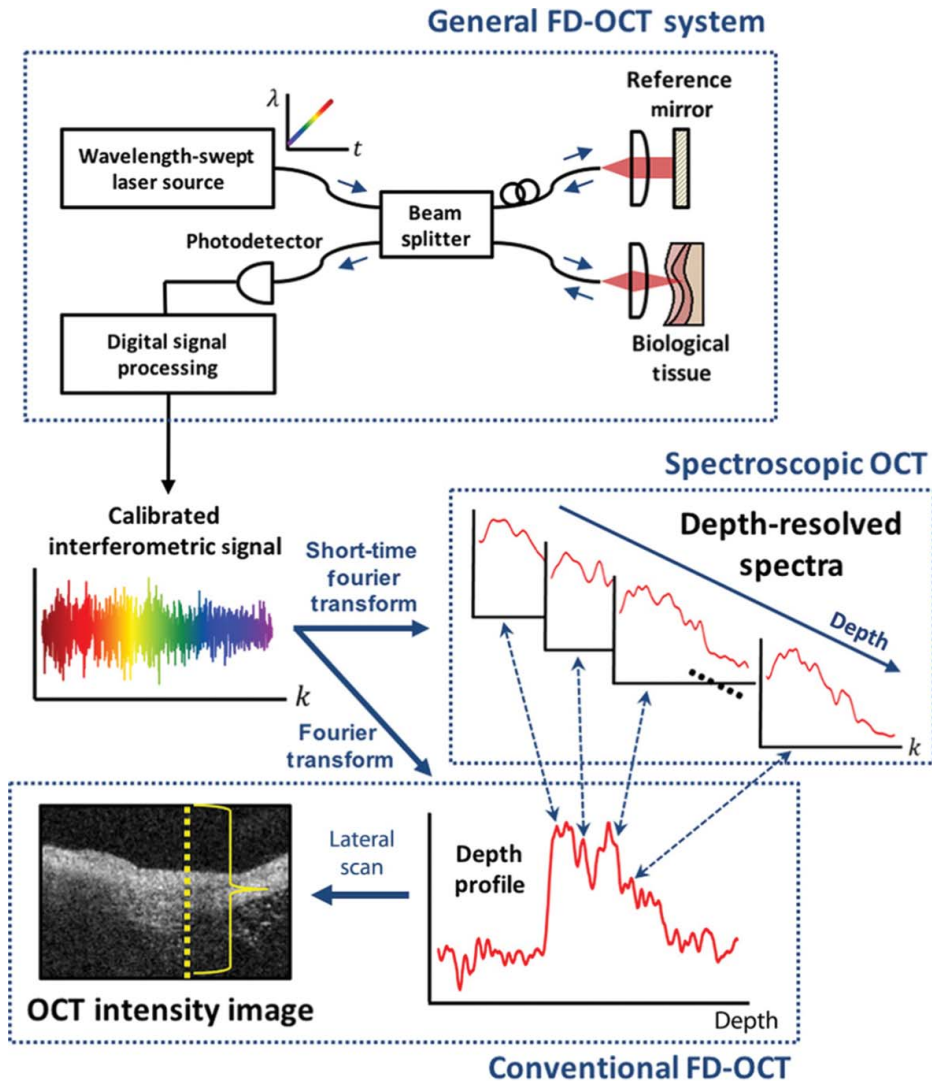


**Figure 1.** Concepts and comparison of conventional FD-OCT and S-OCT (reprinted with permission from Nam et al. (80); Copyright 2016 Society of Photo Optical Instrumentation Engineers).

Fourier-transform:

$$F(z) = \mathcal{F}[I_{int}(k)] = \int_{-\infty}^{\infty} I_{int}(k) e^{-ikz} dk \quad (1)$$

where  $I_{int}(k)$  is the interferogram with wavenumber,  $k$ , and  $F(z)$  is the axial intensity profile of the sample along the direction of depth,  $z$ .

Advances in FD-OCT have enabled its application to diagnostic medicine and pathological research in various medical fields (6), including ophthalmology (7, 8), dermatology (9, 10), and cardiology (11–13). However, standalone gray-scale OCT images, which provide only morphological information, do not fully represent the pathological changes of a lesion.

Generally, pathological changes in a lesion are accompanied by changes in biochemical properties as well as morphological features. In this way, the absence of biochemical properties limits the diagnostic performance of the gray-scale OCT images. While reviews on general OCT technology development and applications have been published (2, 6, 14), extensive reviews on spectroscopic OCT and its biomedical applications have not yet been reported. Thus, in this article, we present a comprehensive review of the post-processing technique of spectroscopic OCT (S-OCT) (15, 16), which provides spectroscopic information of a sample by time–frequency analysis (TFA) of an interferogram of OCT. In addition, we review the concepts underlying S-OCT, signal processing strategies and methods, and biomedical applications in various medical fields.

### Spectroscopic OCT: Time–frequency analysis of an interferogram

S-OCT is an extension of OCT that allows depth-resolved spectroscopic analysis of a sample within the spectral range of the broadband light source of the OCT system. Broadly speaking, S-OCT can be performed in one of two ways: hardware-based and software-based. Hardware-based S-OCT employs two or more light sources with different bands of wavelength and collects the light separately (17–19). Thus, hardware-based S-OCT enables spectroscopic analysis based on multiple light sources comprising distinct wavelength bands.

In this review, we only discuss software-based S-OCT, which does not require hardware modification of the typical OCT system. Spectroscopic analysis for software-based S-OCT can be accomplished by time–frequency transformation (TFT) of OCT interferograms (Figure 1). Therefore, software-based S-OCT can provide not only a depth-resolved structure of a sample, but also spectroscopic information for a specific depth within the band of the light source, both of which can be obtained simultaneously using a post-processing technique and any FD-OCT system. In other words, with S-OCT, backscattering spectra containing spectroscopic properties of the sample, such as wavelength-dependent absorption and scattering, are provided for every pixel in an OCT image of a sample without any additional hardware requirements.

Since spectroscopic information obtained by S-OCT is derived from interferograms of OCT, S-OCT inherits the advantages of OCT described above. Therefore, spectroscopic analysis in conjunction with gray-scale OCT images can alleviate the limitations of OCT application in diagnostic medicine and pathological research, such as lesion identification and classification of tissue components.

TFT of interferograms allows for spectroscopic analysis of the OCT signal. Recent research into S-OCT relied on two common methods for TFT: short-time Fourier transform (STFT) and the dual window (DW) method (20). STFT, a type of linear TFT, is the classically and commonly used method for TFA and is also called windowed Fourier transform:

$$S(k, z) = \text{STFT}[I_{\text{int}}(k)] = \int_{-\infty}^{\infty} I_{\text{int}}(k') w(k' - k; \Delta k) e^{-ik'z} dk' \quad (2)$$

where  $w(k)$  is a window function with spectral bandwidth  $\Delta k$ . The fixed window  $w(k)$  slides incrementally onto an interferogram, the sections confined by the window are

Fourier-transformed, and a time–frequency distribution (TFD) by STFT is subsequently generated. The advantages of STFT include that it is artifact-free, relatively simple to perform, and generally has good performance. However, STFT suffers from the uncertainty principle, in that there is a trade-off between spectral and axial resolution introduced by the windowing process. Specifically, use of wider windows generates a TFD with a better axial resolution but a poorer spectral resolution, and vice versa (Figure 2b and c). In addition, the type of window function (e.g., Hanning and Gaussian) is an important factor for determining performance (21, 22). Thus, the optimal size and type of window function should be chosen with great caution according to the intended application.

The DW method described by Robles et al. (23) is a recently developed TFD method that provides a TFD with simultaneously high spectral and axial resolution by multiplying two TFDs by wide and narrow windows, respectively (Figure 2d–f):

$$S_{DW}(k, z) = S_w \left( k, z; w(k) = e^{-\frac{k^2}{2\Delta k_w^2}} \right) S_n \left( k, z; w(k) = e^{-\frac{k^2}{2\Delta k_n^2}} \right) \quad (3)$$

where  $S_w$  is an STFT with a wide Gaussian window having width  $\Delta k_w$ , and  $S_n$  is an STFT with a narrow Gaussian window having width  $\Delta k_n$  ( $\Delta k_b \gg \Delta k_n$ ). Since  $\Delta k_w$  and  $\Delta k_n$  directly determine the spectral and axial resolution of the TFD, respectively, the width of both Gaussian windows should be chosen carefully to identify the optimal spectral and axial resolution. In cases employing two orthogonal Gaussian windows, the DW method can produce a TFD that is mathematically identical to a Wigner–Ville distribution, which is a type of

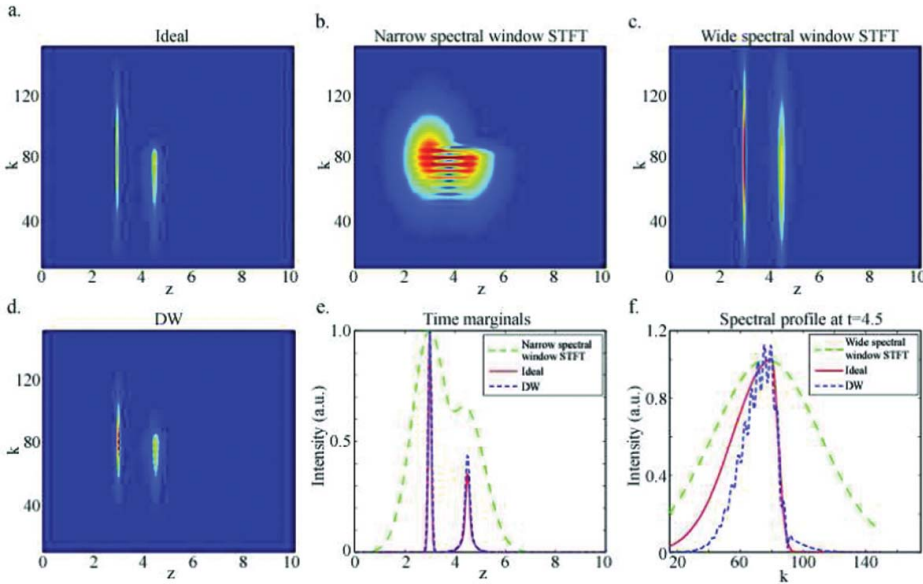


**Figure 2.** Comparison of the performances of the STFT and DW methods. (a) Ideal depth-resolved spectra from two layers with different spectroscopic features. (b) A depth-resolved spectra generated by STFT with a narrow window. (c) A depth-resolved spectra generated by STFT with a wide window. (d) A depth-resolved spectra generated by the DW method exhibiting high spectral and axial resolution. (e, f) Comparison of the three results in terms of axial and spectral resolution (reprinted with permission from Robles et al. (23); Copyright 2009 Optical Society of America).

bilinear TFT or Cohen's class. This bilinear TFT offers a TFD with both high spectral and axial resolution, thereby avoiding the resolution trade-off. However, this approach can suffer from unwanted oscillation artifacts and has a heavy computational burden. A spectrum produced using the DW method can be modulated by wavelength-dependent scattering within a small scattering particle or between particles (24). This modulation can be suppressed by low pass filtering of the spectrum, and the resulting spectrum can provide spectroscopic information about the surrounding tissue.

The method used for TFT and the determination of window type and size have a significant effect on S-OCT performance. Thus, careful consideration of the method and the parameters is necessary and depends on the intended application. Detailed guidelines for choosing an appropriate method are provided in the following section.

### Scale of interest and time–frequency transformation methods

In S-OCT, the TFD determined as  $S(k, z)$  generated by the TFT method introduced in the previous section represents depth-resolved spectra corresponding to a single depth profile,  $I(z)$ , and  $S(k, z_0)$  means the backscattering spectrum at a specific depth  $z_0$ . The backscattering spectra extracted by S-OCT can be analyzed using one of two approaches based on the scale of interest based on the coherence length of the light source. The first approach is interested in the scale above the coherence length, and the goal of this approach is to extract global spectroscopic properties such as wavelength-dependent absorption and scattering from a sample tissue (25–32). The quantitative measurements of these spectroscopic properties allow substance identification and tissue classification. The second approach is interested in the scale below the coherence length, and the goal of this approach is to investigate local-scaled properties such as wavelength-dependent scattering by particles smaller than the coherence length (24, 33, 34). In this approach, the backscattered light from the front and the rear surfaces of the scattering particle can interfere with each other when the size of the particle is less than the coherence length. Since the amplitude of the interference light is wavelength-dependent, the interference can modulate the original spectrum of the light source, and the modulation frequency is proportional to the size of the scattering particle. Thus, scattering particle size can be estimated from the dominant frequency of the modulated spectrum.

Several comparison studies (20–22, 35, 36) have provided guidelines for choosing an optimal TFT method, as its required parameters depend on the given application. Bosschaart et al. (20) evaluated the performance of STFT and the DW method in terms of spectral resolution, axial resolution, and spectral recovery. The authors reported that spectral recovery should be considered in the TFT method, because small deviations in spectral shape can produce large errors in analysis. From a simulation of the quantification of optical absorption property to identify hemoglobin concentration and blood oxygen saturation level, the authors also showed that STFT provides more reliable TFDs than the DW method with respect to spectral recovery, by comparing the  $\chi^2$  value of fitting results with that of a reference spectrum. Unfortunately, adjustment of window sizes to enhance spectral recovery in the DW method sacrifices the resolution benefit of DW method. Based on these findings, the authors concluded that STFT is the optimal method to extract optical properties in bulk tissue for applications such as the quantitative measurement of absorption and scattering coefficients.

Although the DW method is less suitable for applications on a global scale, it can be more accurate and useful for identifying single cell particles compared to STFT (34, 37). As stated in the previous section, the spectral oscillation caused by the interference between the backscattered lights from the particle is included in the spectrum of S-OCT, and the oscillation frequency correlates with the size of the particle. The particle size can be derived and estimated by Fourier-transforming the spectrum, such that the size of the dominant scattering particles can be identified at a single pixel by detecting the first peak position of the Fourier-transformed data (34, 38). The STFT method is not adequate for accomplishing this estimation, as both high spectral and axial resolution are required to reconstruct the size of a particle (Figure 2e and f). Thus, the DW method is more suitable for research interested in local scale measurements of single scattering particles.

### Quantitative measurements and qualitative visualizations

Quantitative measurement of wavelength-dependent attenuation profiles is the main interest of global approaches, which are used to characterize spectroscopic features of a tissue sample. Theoretically, both absorption and scattering contribute to optical attenuation following Lambert–Beer’s law:

$$H_t(k, z) = \exp \left( -2 \int_0^z \mu_t(k, z') dz' \right) = \exp \left( -2 \int_0^z [\mu_s(k, z') + \mu_a(k, z')] dz' \right) \quad (4)$$

where  $H_t$  denotes the wavelength- and depth-resolved attenuation by a sample tissue, the factor 2 denotes the round trip of the illumination light, and  $\mu_t$ ,  $\mu_s$ , and  $\mu_a$  denote the wavelength- and depth-resolved total attenuation, absorption, and scattering coefficients, respectively.

Depth-resolved spectra are generally fitted to the above exponential equation (Eq. (4)) along the depth direction, from which the total attenuation coefficient can be calculated. However, the total attenuation coefficient is a summation of absorption and scattering coefficients, which are independent of each other. Separation of absorption and scattering contribution can thus be useful for characterizing the spectroscopic features of a sample tissue. Indeed, several studies have described extracting absorption and scattering coefficients from spectra by S-OCT. In one example, Hermann et al. (25) extracted absorption profiles from a homogeneous phantom with small absorbers embedded in weakly scattering media in which light scattering could be neglected. The authors could extract quantitative absorption profiles with fairly high precision within a wavelength range equivalent to the full width at half maximum (FWHM) of the light source. However, this study was limited by the fact that biological tissue is a highly scattering media, and light scattering is more dominant than absorption by several orders of magnitude.

Several additional studies have focused on simultaneous extraction of absorption and scattering profiles. Bosschaart et al. (28) extracted absorption profiles of a green absorbing dye from phantoms with different concentrations of polystyrene scattering particles. Xu et al. (26) developed an algorithm based on a least-squares method to separate absorption and scattering contributions with the assumption that the absorption spectrum of the dominant absorbers in a sample were known *a priori*, and that the absorption spectrum was very



different from the scattering spectrum of the tissue media. The authors validated the algorithm for single-layered and multi-layered phantoms with a NIR absorbing dye. However, all of the aforementioned studies required *a priori* information about either absorption or scattering profile, such that separation was not possible without *a priori* information.

Recently, Robles et al. (29) developed an analytical method to separate absorption and scattering coefficients that does not require any *a priori* information. Specifically, the authors analyzed the nonlinear phase term of an interferogram related to the dispersion of a sample tissue and determined the real part of the refractive index from the nonlinear phase term. Using Kramers–Kronig relations such that the imaginary part of a complex analytic function signal can be calculated from the real part and vice versa, the authors could calculate the imaginary part of the refractive index, which is proportional to the absorption coefficient of a sample tissue. In other words, the absorption coefficient can be determined from the nonlinear phase term. In addition, the authors showed that the total attenuation coefficient ( $\mu_t = \mu_a + \mu_s$ ) can be measured from the TFD of an interferogram, and that the scattering coefficient can be subsequently calculated by simple subtraction,  $\mu_s = \mu_t - \mu_a$ .

Efforts to quantitatively measure absorption and scattering coefficients based on S-OCT allow depth-resolved quantitative analyses for spectroscopic information in various applications, especially measurement of hemoglobin concentration and blood oxygen saturation level (39–51). However, quantitative analysis in the full axial range is challenging because of the limited penetration depth inherent to OCT. Thus, for some applications, qualitative visualization of spectroscopic information based on a color map is preferred.

Jaedicke et al. (52) proposed a metrics analysis for interpretation of spectra to visualize and highlight spectroscopic properties of a sample. In their work, “metric” does not refer to a specific quantitative value, but rather a single value that only represents spectroscopic properties. Thus, their method of analysis focuses on qualitative visualization of the spectroscopic properties of a sample by color-coding rather than measuring quantitative spectroscopic properties such as absorption and scattering coefficients (Figure 3). The purpose of this approach is to reduce the dimensionality of spectra to 1-to-3 dimensions in order to visualize and emphasize spectroscopic properties using a pseudo-color map overlaid on an original OCT image. Generally, the hue-saturation-value (HSV) color-space is used for this color-coding. In the color-space, a metric is assigned to the hue channel as color and an original OCT image is assigned to the value channel as brightness to simultaneously describe spectroscopic and morphological features. The authors introduced several different representative metrics, including COM (center of mass), SUB-RGB (sub-band red green blue), PCA-RGB (principal component analysis red green blue), ACF (autocorrelation function), and PHA (phasor analysis). The COM metric, calculated by the center of mass for each spectrum, is the simplest metric in the analysis to extract a representative single value from the spectrum (15). SUB-RGB is a metric similar in concept to the way the human eye perceives light. Specifically, the spectrum is divided into three sub-bands by weighting functions, and the summed value of each sub-band is assigned to the red, green, and blue of the RGB color-space, respectively (38, 47). PCA-RGB is calculated by taking the three main principal components of the spectrum to reduce the dimensionality, and the resultant coefficients of each principal component are encoded to red, green, and blue of the RGB color-space, respectively (53). ACF and PHA are metrics used to indicate the scattering properties of a sample in the local scale. ACF is a metric calculated from the autocorrelation function of the spectrum (54, 55), and PHA reduces the spectrum into two values, the real and imaginary parts

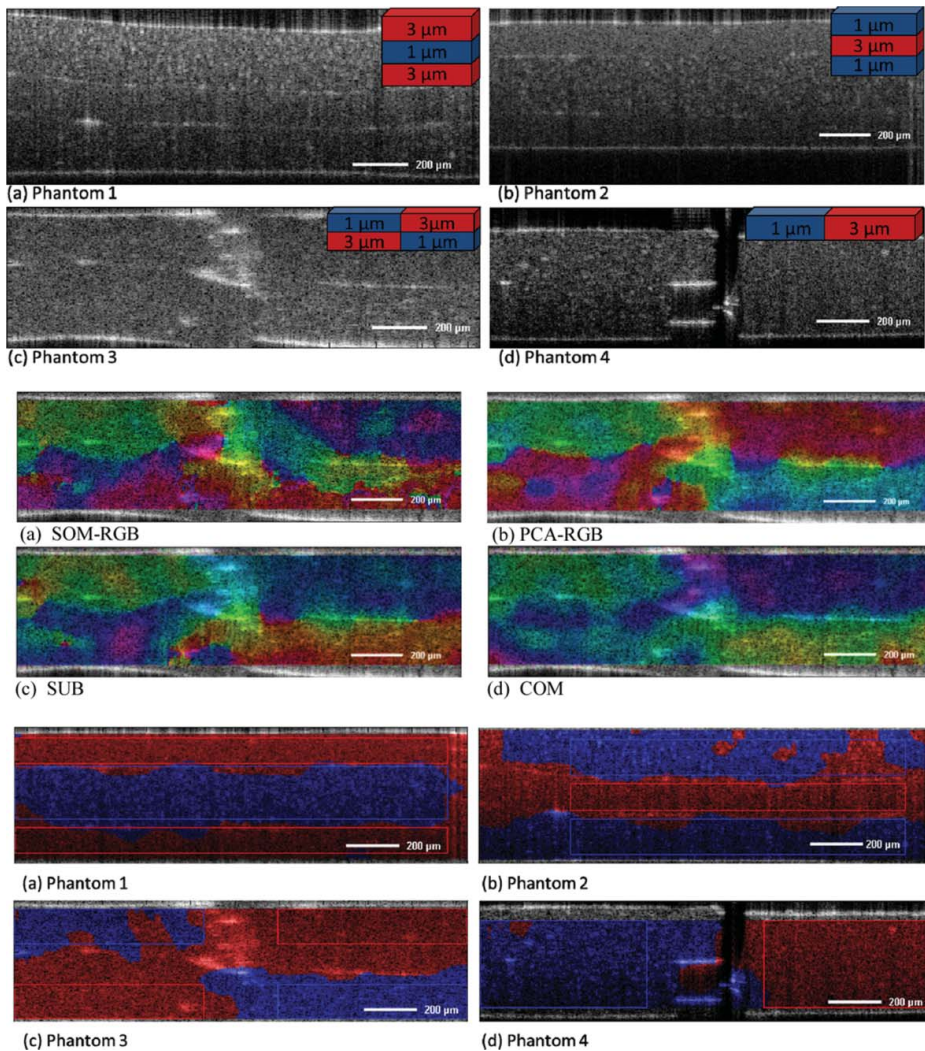


**Figure 3.** Metric analysis demonstrated with phantoms containing different sizes of microspheres. The first two rows represent the gray-scale OCT images of phantoms. The following two rows represent the color-coded OCT images of the phantom by the metrics SOM-RGB, PCA-RGB, SUB-RGB, and COM, respectively. The last two rows represent the color-coded OCT images by the classification results according to *K*-means clustering based on the PCA metric. Clear characterization of the areas with different microspheres is visible in the overlaid images (reprinted with permission from Jaedicke et al. (52); Copyright 2013 Optical Society of America).

of the Fourier-transformation of the spectrum at a particular frequency (56, 57). In addition, the authors used pattern recognition methods based on the metrics to characterize and separate the area with different spectroscopic properties, including *K*-means clustering (58), self-organizing maps (SOM) (59), and support vector machine (SVM) (60). The authors also demonstrated that SVM classification with PCA-RGB generate a result with the best performance for the classification of phantoms with different sizes of microspheres. However, since the performance of classification using metrics analysis differs according to the specific application, the choice of metrics in the analysis is very important. Nevertheless, metric



analysis combined with a pattern recognition algorithm could be a useful tool to qualitatively visualize spectroscopic properties and characterize sample features in biological tissues regardless of the scale of interest.

### Measurement of hemoglobin concentration and blood oxygen saturation level

The most widely used application of S-OCT (39–51) is measurement of hemoglobin (Hb) concentration and blood oxygen saturation levels ( $\text{SO}_2$ ), which are important biomarkers strongly related to various pathological changes such as tumor progression (61) and ophthalmological degeneration (62, 63). In contrast with modalities measuring  $\text{SO}_2$  such as functional near-infrared spectroscopy (fNIRS) (64, 65), functional magnetic resonance imaging (fMRI) (66), fluorescence lifetime imaging microscopy (FLIM) (67), and photoacoustic microscopy (PAM) (68, 69), S-OCT has the ability to provide depth-resolved spectroscopic information with high spatial resolution in a non-contact and non-invasive manner. By analyzing the spectroscopic information provided by S-OCT, quantitative measurement of Hb concentration and  $\text{SO}_2$  can be achieved.

Studies employing fNIRS and fMRI generally utilize a wavelength band ranging from 750 nm to 850 nm, which contains the isosbestic point near 800 nm (70), (Figure 4a). This very distinct absorption feature enables quantitative measurement of  $\text{SO}_2$ , defined as the percentage of oxy-Hb concentration to the total Hb concentration (oxy-Hb + deoxy-Hb). Likewise, the same wavelength band can be used for S-OCT (39–43).

Faber et al. (39) demonstrated the feasibility of using S-OCT to quantitatively measure the absorption coefficients of oxy-Hb and deoxy-Hb. Specifically, the authors acquired spectroscopic information of weakly-scattering oxy-Hb and deoxy-Hb solutions and subsequently measured the absorption coefficients of oxy-Hb and deoxy-Hb by fitting the depth-resolved spectra using the function described in Eq. (4). The resultant measured absorption spectrum was in good agreement with the literature. Later, Faber et al. (40) conducted a similar

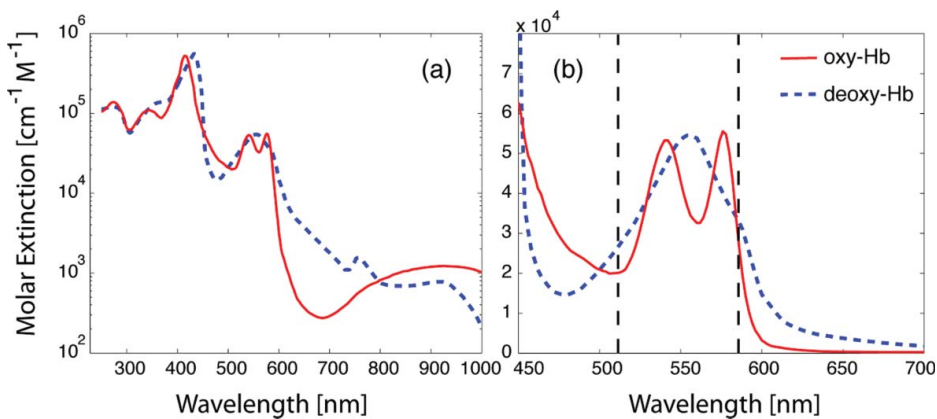


**Figure 4.** (a) The absorption spectra of oxy-Hb and deoxy-Hb on the band from visible light to near-infrared. The isosbestic point of both spectra is shown around 800 nm. (b) Absorption in the visible band is dominant to that in the near-infrared region. The absorption spectra within the black dotted lines in (b) are the most distinguishable from each other, since the spectra are independent of each other, having a correlation coefficient of zero (reprinted with permission from Robles et al. (44); Copyright 2010 Optical Society of America).

experiment with strongly scattering whole blood not diluted by water in order to take into account both absorption and scattering. The authors estimated scattering coefficients of oxy-Hb and deoxy-Hb based on the separation method described in the previous section (29) and found that both oxy-Hb and deoxy-Hb had the same wavelength-dependent decrease of scattering coefficient with increasing wavelength. In addition, the authors experimentally measured the total attenuation coefficients at 780 nm ( $\mu_{t,780}$ ) and 820 nm ( $\mu_{t,820}$ ) (note that the isosbestic point is near 800 nm.) and calculated the differential attenuation coefficient ( $\mu_{t,820} - \mu_{t,780}$ ) from phantoms for different values of  $\text{SO}_2$ . By comparing the differential attenuation coefficients versus  $\text{SO}_2$ , a clear negative correlation was identified, and the differential attenuation coefficient was found to approach zero as  $\text{SO}_2$  increased. This approach revealed that the increasing dependence of the absorption coefficient of oxy-Hb is cancelled out by the dependence of scattering by whole blood. In addition to these studies, Lu et al. (42) assessed  $\text{SO}_2$  by calculating the ratio of the attenuation coefficients from a depth-profile reconstructed by the longer wavelength band to that of the isosbestic point over the shorter wavelength band. Using this approach, the authors were able to assess relative  $\text{SO}_2$  and found that larger ratios were associated with higher  $\text{SO}_2$  values.

Applications of S-OCT based on the near-infrared band are often limited when monitoring  $\text{SO}_2$  in living animals, due to the significant scattering in blood that can disturb quantitative measurements of  $\text{SO}_2$ . As shown in Figure 4, absorption by both oxy-Hb and deoxy-Hb in the visible band ranging from 520 nm to 585 nm is approximately two orders of magnitude larger than that of the near-infrared band, while scattering remains on the same order of magnitude (40). Moreover, the absorption spectra of oxy-Hb and deoxy-Hb are clearly distinguishable from each other, exhibiting a double-peaked spectrum for oxy-Hb at 540 nm and 575 nm and a single-peaked spectrum for deoxy-Hb at 555 nm (Figure 4b). Therefore, since scattering can be neglected, the measurement of Hb concentration and  $\text{SO}_2$  based on the visible light band can generate a more reliable result with higher sensitivity (44–51).

Robles et al. (44) developed an OCT system based on the visible light band to measure Hb concentration and  $\text{SO}_2$  by utilizing the distinguishable absorption spectra of oxy-Hb and deoxy-Hb. Using the spectroscopic information from S-OCT, the authors were able to measure the absorption coefficients of oxy-Hb and deoxy-Hb from phantoms with human ferrous stable Hb by fitting the depth-resolved spectra using the function described in Eq. (4). Specifically, using the measured absorption coefficients, the authors calculated the concentration of oxy-Hb and deoxy-Hb based on the fact  $\mu_a = \varepsilon C_{Hb}$ , where  $\mu_a$  is the absorption coefficient of Hb,  $\varepsilon$  is the known molar extinction coefficient of Hb (70), and  $C_{Hb}$  is the concentration of Hb. The authors compared the measured Hb concentration with the expected concentration and found that both were in excellent agreement, even though the Hb concentration was low. Furthermore, a linear least-squares model based on the depth-resolved spectra was introduced to obtain the concentration of oxy-Hb and deoxy-Hb allowing the quantitative measurement of  $\text{SO}_2$ . Later, Robles et al. (47) confirmed the feasibility of visible light OCT for quantitative measurement of  $\text{SO}_2$  using an *in vivo* mouse model with a dorsal skinfold. The authors also presented a true-color representation using the SUB-RGB metric to provide additional true-color contrast in an intuitive way. As a result, the authors were able to simultaneously show morphological structures in the form of a true-color display, e.g., muscle layer, subcutaneous layer, and lumen of blood vessels including small capillaries, and functional  $\text{SO}_2$  information for each pixel (Figure 5). In addition, monitoring of the effect of exogenous contrast agent in  $\text{SO}_2$  and true-color representation was validated *in vivo*.

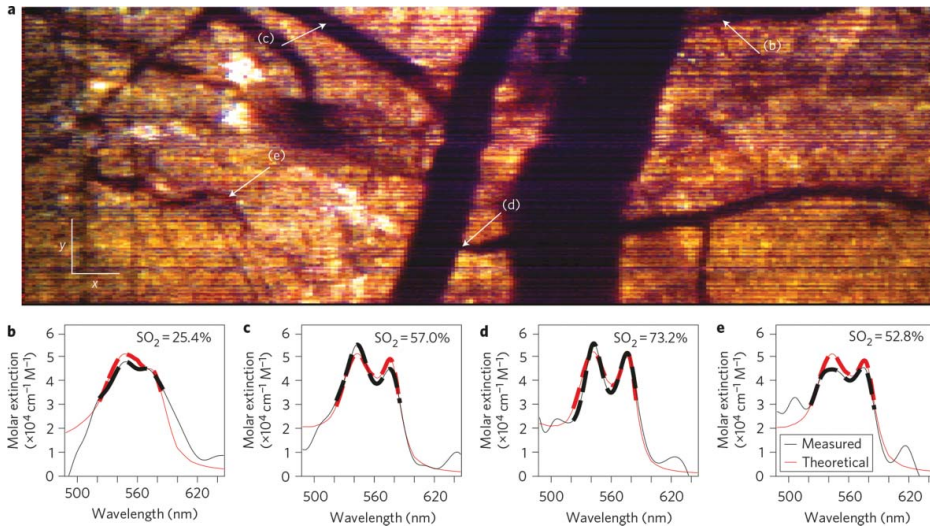


**Figure 5.** (a) *En face* true-color representation of OCT images color-coded by the SUB-RGB metric from the mouse dorsal skinfold. (b–e) Absorption spectra measured by S-OCT from arrows in (a) (reprinted with permission from Robles et al. (47); Copyright 2011 Optical Society of America).

Recently, with the advance of OCT angiography (71–73), the combination of OCT angiography and  $\text{SO}_2$  map deduced by S-OCT has been achieved in the form of overlay pseudo-color  $\text{SO}_2$  maps (48–51), especially in the ophthalmologic field where OCT angiography is most commonly used (48, 50).

### Atherosclerotic plaque detection

Spectroscopic analysis using S-OCT can be extended to the detection of atherosclerotic plaque by investigating the spectroscopic properties of the plaque components. The main interest of this application is characterizing vulnerable plaques with a large lipid-pool and a thin fibrous cap ( $< 65 \mu\text{m}$ ) (74). Catheter-based intravascular OCT systems (13, 75) have the ability to capture the morphological features of such vulnerable plaques. In OCT images, the lipid-pool is described as an area with very high backscattering and high attenuation, while the fibrous tissue is described as an area with high backscattering and low attenuation (76). This distinct features enables visual characterization of atherosclerotic plaques, but its diagnostic performance is limited due to various intrinsic artifacts of intravascular OCT (77). Fortunately, this limitation can be overcome by complementary compositional information provided by spectroscopic analysis using S-OCT.

Fleming et al. (78) demonstrated that the spectroscopic information provided by S-OCT can be used to detect and characterize atherosclerotic plaques. Specifically, the authors created phantoms consisting of cholesterol, collagen, and calcium, which are highly associated with the vulnerability of atherosclerotic plaques (79), and measured wavelength-dependent absorption spectra with a spectrophotometer on the near-infrared band centered at 1,300 nm, the most common band in catheter-based intravascular OCT systems. As shown in Figure 6b, this phantom research showed that cholesterol has a decreasing absorption feature with increasing wavelength, while the other components have relatively featureless

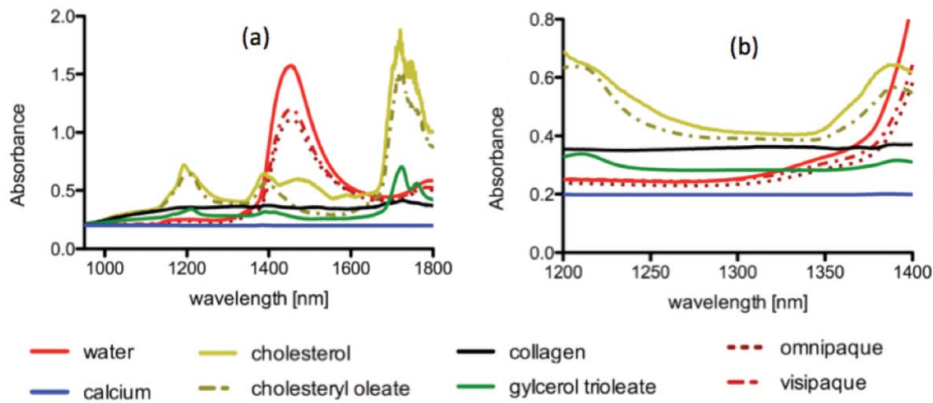


**Figure 6.** (a) Near-infrared absorption spectra of substances related to plaque, such as cholesterol, collagen, and calcium. (b) Magnified spectra of (a) at the wavelength band from 1,200 nm to 1,400 nm (reprinted with permission from Fleming et al. (78); Copyright 2013 Optical Society of America).

absorption spectra throughout the band. In addition, classification of the components was accomplished by quadratic discriminant analysis based on the three main coefficients taken from principal component analysis of the spectra obtained by S-OCT from each phantom. The classification method was able to distinguish cholesterol and non-lipid components and was validated using a swine aorta phantom with a lipid-rich plaque mimic generated with an injection of mayonnaise emulsion.

In this field, we extended the feasibility of S-OCT for detection of lipid-rich plaque to an *in vivo* atherosclerotic animal model using a catheter-based intravascular OCT system (80). Specifically, we utilized metric analysis to describe the spectroscopic properties of lipid based on the novel and robust metric, GCOM (Gaussian COM) metric, which is calculated by taking the mean of the Gaussian fit of each spectrum. Phantom studies with different concentrations of mayonnaise showed that this metric is able to quantify lipid contents, and *in vivo* animal studies using atherosclerotic rabbit model demonstrated the accurate classification of lipid with a sensitivity and specificity of 94% and 77%, respectively (Figure 7).

### Evaluation of burn injuries and assessment of burn severity

The ability of S-OCT to characterize tissues with different spectroscopic properties permits evaluation of burn injuries and assessment of burn severity. Maher et al. (37) evaluated burned animal tissues *in vivo* with S-OCT using power-law fitting and binary logistic regression classification. A mouse model was used for analysis of third-degree burns, which have damage to the epidermis, dermis, and subdermal adipose layers. In their study, each spectrum was fitted to a power-law function,  $A\lambda^{-b}$ , where  $\lambda$  is the wavelength, and  $A$ ,  $b$  are fitted parameters; the resultant fitted parameter  $b$ , the power-law exponent, was used to highlight the spectroscopic difference between healthy and burned tissues (Figure 8c). This approach utilizes the same concept of metric analysis based on the metric of “power-law exponent.” The fitted power-law exponents are distributed at a lower level in burned tissues compared to healthy tissues, because exposed adipose cells in burned tissues cause the spectra to oscil-



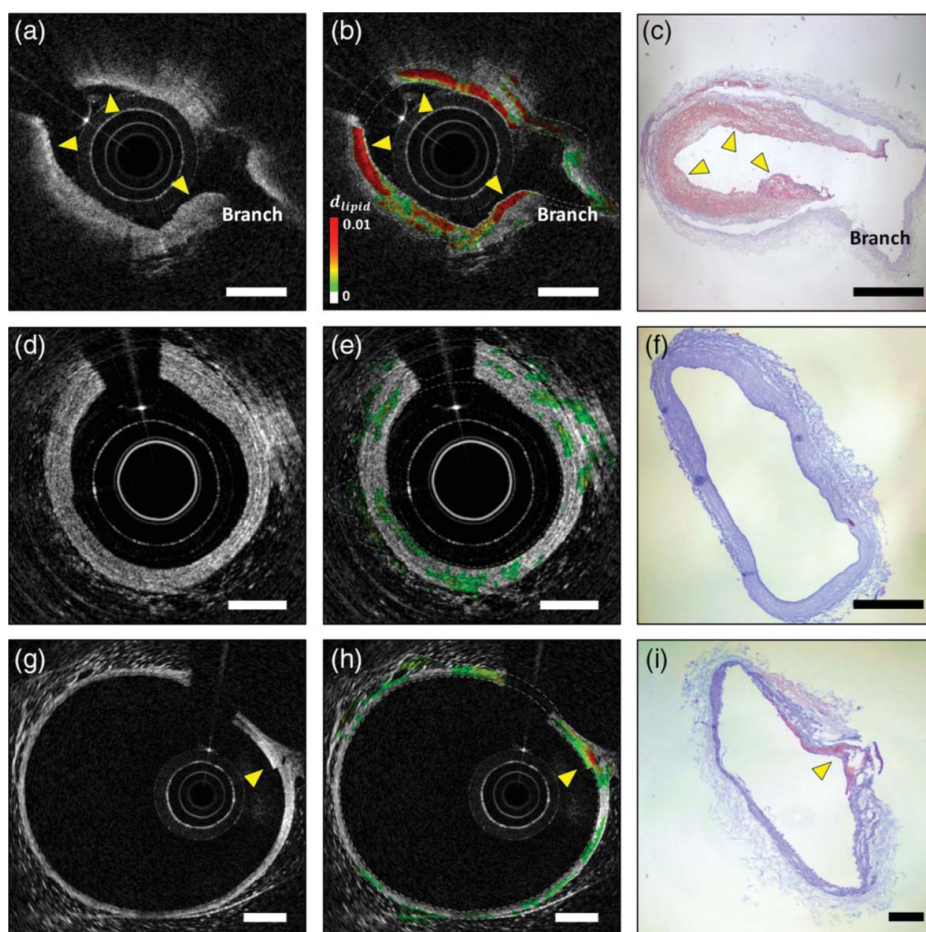


**Figure 7.** Representative results of mapping the lipid distribution function derived from the GCOM metric. The first, second, and third rows show the results for lipid-rich plaques (a–c), fibrous plaques (d–f), and normal tissue (g–i), respectively. Gray-scale OCT images (a), (d), (g) provide morphology only, while the color-coded OCT images by the lipid distribution function (b), (e), (h) provide information about lipid composition, which were in good agreement with ORO-stained histopathological images (c), (f), (i), in which lipids are stained in red. Scale bars, 500  $\mu\text{m}$  (reprinted with permission from Nam et al. (80); Copyright 2016 Society of Photo Optical Instrumentation Engineers).

late and flatten (81) (Figure 8d). To distinguish burned tissues from healthy tissues, a binary logistic regression classification model based on the power-law exponent metric was used (Figure 8e–h), generating accuracies around 91%.

Zhao et al. (82) later assessed burn severity using *in vivo* mouse models with four different levels of burn injury, namely, epidermal burn (EB), superficial partial thickness burn (SPTB), deep partial thickness burn (DPTB), and full thickness burn (FTB). The analysis approach described above was used to assess the severity of burns, and the authors found that increasing severity of burn injury was associated with lower power-exponent values. Logistic regression classification to distinguish burned tissues from healthy tissues showed classification accuracies of 98%, 88%, 90%, and 59% for the FTB, DPTB, SPTB, and EB, respectively, in the surface layer (0–25  $\mu\text{m}$  depth).



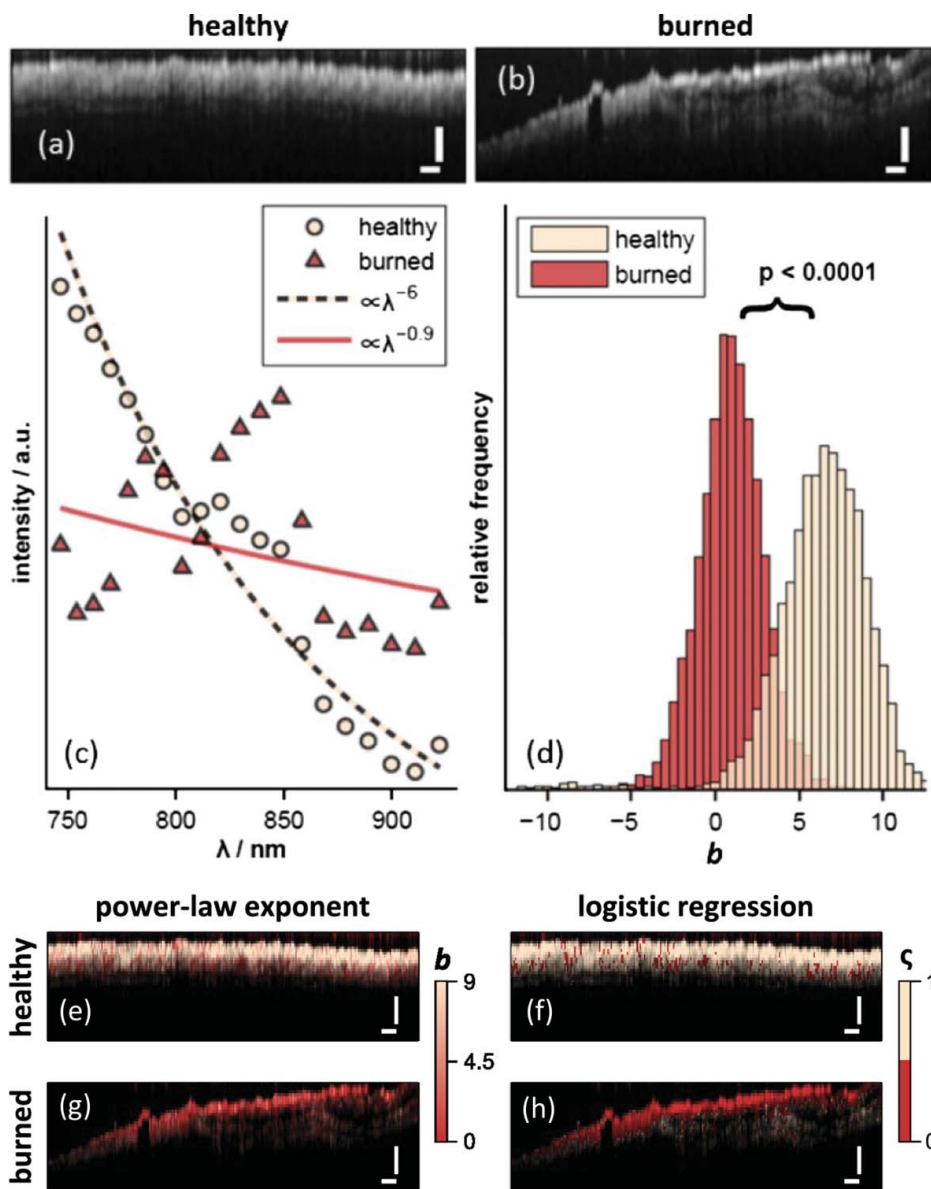


**Figure 8.** (a, b) Representative OCT images of healthy and burned tissues. (c) Representative spectra obtained by S-OCT from healthy and burned tissues. (d) Distributions of the fitted parameter, power-law exponent, from healthy and burned tissues. (e, g) Color-coded OCT images according to the value of the power-law exponent. (f, h) Color-coded OCT images according to the classification results of binary logistic regression based on the power-law exponent (reprinted with permission from Maher et al. (37); Copyright 2014 Optical Society of America).

### Contrast enhancement using S-OCT by exogenous contrast agents

In this section, we will introduce S-OCT applications using exogenous dyes that actively react in the NIR band (83) to maximize the difference in spectroscopic properties between target materials and background for better contrast. Xu et al. (84) demonstrated that NIR

absorbing dyes can enhance contrast in S-OCT with an OCT system in the 780 nm band. In a phantom study using a NIR absorbing dye with its absorption peak at 740 nm, the authors identified a spectral redshift by the dye absorption. In addition, S-OCT was able to quantitatively measure the absorption according to the concentration of the dye.

Recently, advances in nanotechnology have led to studies to improve the contrast of OCT using gold nanostructures, such as gold nanoparticles (85, 86), nanocages (87), and nanorods (88). Gold nanostructures exhibit unique optical properties due to surface plasmon resonance, which can be controlled by their size and geometry (89). They are mainly tuned to a form that exhibits strong absorption in the NIR band, when used as a contrast dye for OCT imaging. Likewise, gold nanostructures can also be used to enhance the contrast in S-OCT applications (90–93). Cang et al. (90) experimentally demonstrated a contrast improvement in S-OCT using gold nanocages with the strong surface plasmon resonance peak at 716 nm by a phantom study. Furthermore, Oldenburg et al. (92) demonstrated the feasibility of using gold nanostructures as contrast agents for S-OCT in biological systems by visualizing human breast carcinoma *ex vivo* using gold nanorods with a plasmon resonance peak at 755 nm.

The advantage of greater contrast provided by gold nanostructures makes it a very attractive approach to S-OCT applications, but challenges remain to be addressed: biocompatibility of the nanostructures (94, 95), and optimization of size and geometry to overcome the limitation of penetration depth due to strong absorption by the nanostructures.

### Applications in the local scale: Precancerous lesion detection

The development of cancer starts with the growth and proliferation of a few abnormal cells. Thus, it is of great importance to detect precancerous development at an early stage and at a cellular level in order to achieve enhanced therapeutic efficacy and reduction in morbidity and mortality. The conventional gold standard for detecting precancerous lesions is histopathological evaluation of a biopsy specimen; however, this approach suffers from sampling error, invasiveness, long procedure time to diagnosis, and intra- and inter-observer variability with respect to biopsy analysis. Thus, S-OCT may represent an alternative modality to detect precancerous lesions since S-OCT is able to determine the size of a scattering particle in specific layers. For example, S-OCT can be used to measure the diameter of enlarged cell nuclei, a key biomarker for precancerous changes (96). Indeed, Graf et al. (97) used this approach to show that S-OCT can be used to assess cell morphology and measure the diameter of cell nuclei. From a sample with monolayer T84 epithelial cells, the authors obtained spectra with local oscillations caused by interference between scattered lights from the front and rear surfaces of nuclei. Since the optical path length difference between the two lights and the oscillation frequency are proportional to the size of cell nuclei, the size of cell nuclei was determined by taking the first peak frequency of the Fourier-transformation of the spectra, which is equal to  $2nd$ , where the factor of 2 accounts for the double-pass of light propagation in the cell nuclear,  $n$  is the refractive index of the cell nuclear, and  $d$  is the diameter of the cell nuclear. Importantly, the authors showed that the diameters measured with S-OCT corresponded with those measured with confocal microscopy with a very small standard deviation.

The same method was later used to measure the diameter of cell nuclei for the detection of precancerous lesions and has since been applied to various cancer animal models. (98, 99) Graf et al. (98) demonstrated the feasibility of the S-OCT method using an *ex vivo* hamster

cheek pouch carcinogenesis model. Specifically, spectra with both high spectral and axial resolution given by the DW method were obtained from healthy and dysplastic tissues in the basal layer of the epithelium. The measured diameters from both tissues were in good agreement with the expected diameters from the literature and were statistically different from each other, suggesting that the diameters of the cell nuclei from dysplastic tissues are significantly larger than those from healthy tissues. In addition, the measurement of the diameter of cell nuclei for the detection of precancerous lesions using S-OCT is compatible with visualization of precancerous structural changes, such as thickening the basal layer, via OCT images.

Thus, this cellular imaging capability of S-OCT has several advantages. First, since it inherits all of the benefits of OCT, it can quickly provide cross-sectional images of cancerous lesions or suspected cancer tissues in a non-invasive manner, enabling the observation of dysplastic alteration of tissue. Second, it can contribute to enhancing the accuracy and reliability of cancer diagnosis by providing additional information on the nucleus size of cells that cannot be identified with conventional OCT. However, the performance of the technique may be limited by uncertainty arising from an incomplete assumption that the refractive indices of the nucleus and surrounding tissues are different from each other and each value is constant. Despite its limitations, the comprehensive information provided by the technique can be helpful for cancer diagnosis, opening up new insights into future cancer research. Furthermore, if it is used in conjunction with OCT angiography, neoangiogenesis imaging as well as nucleus assessment will be allowed in a single OCT imaging, becoming a more powerful technique for assessing cancerous lesion.

## Conclusions

S-OCT is a post-processing technique performed on OCT interferograms that allows for spectroscopic analysis of specific layers of a sample. The depth-resolved backscattering spectra provided by S-OCT contain wavelength-dependent absorption and scattering information about a sample, which can be quantitatively measured by fitting the spectra. These measured spectroscopic properties have been shown to be useful for several applications such as detection of biological components with dominant or unique features of absorption and scattering in samples, including hemoglobin, lipid in atherosclerotic plaques, and burned tissues. Furthermore, local oscillations by small scattering particles in the depth-resolved spectra can be used to estimate the size of the particles, enabling detection of precancerous lesions using S-OCT.

Over the last decade, OCT has become a well-established imaging technique for various medical fields due to its advantages of being non-invasive and having both fast imaging speed and high resolution. Presently, we expect that, in combination with the advantages of gray-scale OCT images, the ability of S-OCT, which can be achieved by post-processing without any hardware modification, to provide spectroscopic information of samples will become a powerful tool to enhance diagnostic performance and facilitate pathological research.

## Funding

This work was supported by the National Research Foundation of Korea (NRF) grant funded by the Korean government (MSIP) (NRF-2015R1A1A1A05027209).

## References

1. Huang, D., Swanson, E. A., Lin, C. P., Schuman, J. S., Stinson, W. G., Chang, W., Hee, M. R., Flotte, T., Gregory, K., Puliafito, C. A., and Fujimoto, J. G. (1991) Optical coherence tomography. *Science* 254(5035): 1178–1181.
2. Drexler, W., Liu, M., Kumar, A., Kamali, T., Unterhuber, A., and Leitgeb, R. A. (2014) Optical coherence tomography today: speed, contrast, and multimodality. *J. Biomed. Opt.* 19(7): 071412.
3. Yun, S., Tearney, G., de Boer, J., Iftimia, N., and Bouma, B. (2003) High-speed optical frequency-domain imaging. *Opt. Express* 11(22): 2953–2963.
4. Yun, S., Tearney, G., Bouma, B., Park, B., and de Boer, J. (2003) High-speed spectral-domain optical coherence tomography at 1.3  $\mu\text{m}$  wavelength. *Opt. Express* 11(26): 3598–3604.
5. Leitgeb, R., Hitzinger, C., and Fercher, A. (2003) Performance of Fourier domain vs. time domain optical coherence tomography. *Opt. Express* 11(8): 889–894.
6. Zysk, A. M., Nguyen, F. T., Oldenburg, A. L., Marks, D. L., and Boppart, S. A. (2007) Optical coherence tomography: a review of clinical development from bench to bedside. *J. Biomed. Opt.* 12(5): 051403.
7. Hee, M. R., Izatt, J. A., Swanson, E. A., Huang, D., Schuman, J. S., Lin, C. P., Puliafito, C. A., and Fujimoto, J. G. (1995) Optical coherence tomography of the human retina. *Arch. Ophthalmol.* 113(3): 325–332.
8. Puliafito, C. A., Hee, M. R., Lin, C. P., Reichel, E., Schuman, J. S., Duker, J. S., Izatt, J. A., Swanson, E. A., and Fujimoto, J. G. (1995) Imaging of macular diseases with optical coherence tomography. *Ophthalmology* 102(2): 217–229.
9. Gambichler, T., Moussa, G., Sand, M., Sand, D., Altmeyer, P., and Hoffmann, K. (2005) Applications of optical coherence tomography in dermatology. *J. Dermatol. Sci.* 40(2): 85–94.
10. Welzel, J. (2001) Optical coherence tomography in dermatology: A review. *Skin Res. Technol.* 7(1): 1–9.
11. Tearney, G. J., Brezinski, M. E., Bouma, B. E., Boppart, S. A., Pitris, C., Southern, J. F., and Fujimoto, J. G. (1997) In vivo endoscopic optical biopsy with optical coherence tomography. *Science* 276(5321): 2037–2039.
12. Tearney, G. J., Waxman, S., Shishkov, M., Vakoc, B. J., Suter, M. J., Freilich, M. I., Desjardins, A. E., Oh, W. Y., Bartlett, L. A., Rosenberg, M., and Bouma, B. E. (2008) Three-dimensional coronary artery microscopy by intracoronary optical frequency domain imaging. *JACC Cardiovasc. Imaging* 1(6): 752–761.
13. Yun, S. H., Tearney, G. J., Vakoc, B. J., Shishkov, M., Oh, W. Y., Desjardins, A. E., Suter, M. J., Chan, R. C., Evans, J. A., Jang, I. K., Nishioka, N. S., de Boer, J. F., and Bouma, B. E. (2006) Comprehensive volumetric optical microscopy in vivo. *Nat. Med.* 12(12): 1429–1433.
14. Yang, C. (2005) Molecular contrast optical coherence tomography: A review. *Photochem. Photobiol.* 81(2): 215–237.
15. Morgner, U., Drexler, W., Kartner, F. X., Li, X. D., Pitris, C., Ippen, E. P., and Fujimoto, J. G. (2000) Spectroscopic optical coherence tomography. *Opt. Lett.* 25(2): 111–113.
16. Leitgeb, R., Wojtkowski, M., Kowalczyk, A., Hitzinger, C. K., Sticker, M., and Fercher, A. F. (2000) Spectral measurement of absorption by spectroscopic frequency-domain optical coherence tomography. *Opt. Lett.* 25(11): 820–822.
17. Kim, T. S., Jang, S. J., Oh, N., Kim, Y., Park, T., Park, J., and Oh, W. Y. (2014) Dual-wavelength band spectroscopic optical frequency domain imaging using plasmon-resonant scattering in metallic nanoparticles. *Opt. Lett.* 39(10): 3082–3085.
18. Tanaka, M., Hirano, M., Murashima, K., Obi, H., Yamaguchi, R., and Hasegawa, T. (2015) 1.7- $\mu\text{m}$  spectroscopic spectral-domain optical coherence tomography for imaging lipid distribution within blood vessel. *Opt. Express* 23(5): 6645–6655.
19. Yu, L., Kang, J., Jinata, C., Wang, X., Wei, X., Chan, K. T., Lee, N. P., and Wong, K. K. (2015) Tri-band spectroscopic optical coherence tomography based on optical parametric amplification for lipid and vessel visualization. *J. Biomed. Opt.* 20(12): 126006.
20. Bosschaart, N., van Leeuwen, T. G., Aalders, M. C., and Faber, D. J. (2013) Quantitative comparison of analysis methods for spectroscopic optical coherence tomography. *Biomed. Opt. Express* 4(11): 2570–2584.

21. Bosschaart, N., van Leeuwen, T. G., Aalders, M. C., and Faber, D. J. (2014) Quantitative comparison of analysis methods for spectroscopic optical coherence tomography: reply to comment. *Biomed. Opt. Express* 5(9): 3034–3035.
22. Kraszewski, M., Trojanowski, M., and Strakowski, M. R. (2014) Comment on “Quantitative comparison of analysis methods for spectroscopic optical coherence tomography. *Biomed. Opt. Express* 5(9): 3023–3033.
23. Robles, F., Graf, R. N., and Wax, A. (2009) Dual window method for processing spectroscopic optical coherence tomography signals with simultaneously high spectral and temporal resolution. *Opt. Express* 17(8): 6799–6812.
24. Wax, A., Yang, C., and Izatt, J. A. (2003) Fourier-domain low-coherence interferometry for light-scattering spectroscopy. *Opt. Lett.* 28(14): 1230–1232.
25. Hermann, B., Bizheva, K., Unterhuber, A., Povazay, B., Sattmann, H., Schmetterer, L., Fercher, A., and Drexler, W. (2004) Precision of extracting absorption profiles from weakly scattering media with spectroscopic time-domain optical coherence tomography. *Opt. Express* 12(8): 1677–1688.
26. Xu, C. Y., Marks, D. L., Do, M. N., and Boppart, S. A. (2004) Separation of absorption and scattering profiles in spectroscopic optical coherence tomography using a least-squares algorithm. *Opt. Express* 12(20): 4790–4803.
27. Storen, T., Royset, A., Svaasand, L. O., and Lindmo, T. (2005) Functional imaging of dye concentration in tissue phantoms by spectroscopic optical coherence tomography. *J. Biomed. Opt.* 10(2): 024037.
28. Bosschaart, N., Aalders, M. C., Faber, D. J., Weda, J. J., van Gemert, M. J., and van Leeuwen, T. G. (2009) Quantitative measurements of absorption spectra in scattering media by low-coherence spectroscopy. *Opt. Lett.* 34(23): 3746–3748.
29. Robles, F. E., and Wax, A. (2010) Separating the scattering and absorption coefficients using the real and imaginary parts of the refractive index with low-coherence interferometry. *Opt. Lett.* 35(17): 2843–2845.
30. Kasseck, C., Jaedicke, V., Gerhardt, N. C., Welp, H., and Hofmann, M. R. (2010) Substance identification by depth resolved spectroscopic pattern reconstruction in frequency domain optical coherence tomography. *Opt. Commun.* 283(23): 4816–4822.
31. Bosschaart, N., Faber, D. J., van Leeuwen, T. G., and Aalders, M. C. (2011) Measurements of wavelength dependent scattering and backscattering coefficients by low-coherence spectroscopy. *J. Biomed. Opt.* 16(3): 030503.
32. Ho, T. S., Yeh, P., Tsai, C. C., Hsu, K. Y., and Huang, S. L. (2014) Spectroscopic measurement of absorptive thin films by spectral-domain optical coherence tomography. *Opt. Express* 22(5): 5675–5683.
33. Xu, C., Carney, P., and Boppart, S. (2005) Wavelength-dependent scattering in spectroscopic optical coherence tomography. *Opt. Express* 13(14): 5450–5462.
34. Robles, F. E., and Wax, A. (2010) Measuring morphological features using light-scattering spectroscopy and Fourier-domain low-coherence interferometry. *Opt. Lett.* 35(3): 360–362.
35. Xu, C., Kamalabadi, F., and Boppart, S. A. (2005) Comparative performance analysis of time-frequency distributions for spectroscopic optical coherence tomography. *Appl. Opt.* 44(10): 1813–1822.
36. Graf, R. N., and Wax, A. (2007) Temporal coherence and time-frequency distributions in spectroscopic optical coherence tomography. *J. Opt. Soc. Am. A: Opt. Image Sci. Vis.* 24(8): 2186–2195.
37. Maher, J. R., Jaedicke, V., Medina, M., Levinson, H., Selim, M. A., Brown, W. J., and Wax, A. (2014) In vivo analysis of burns in a mouse model using spectroscopic optical coherence tomography. *Opt. Lett.* 39(19): 5594–5597.
38. Xu, C., Vinegoni, C., Ralston, T. S., Luo, W., Tan, W., and Boppart, S. A. (2006) Spectroscopic spectral-domain optical coherence microscopy. *Opt. Lett.* 31(8): 1079–1081.
39. Faber, D. J., Mik, E. G., Aalders, M. C., and van Leeuwen, T. G. (2003) Light absorption of (oxy-) hemoglobin assessed by spectroscopic optical coherence tomography. *Opt. Lett.* 28(16): 1436–1438.
40. Faber, D. J., Mik, E. G., Aalders, M. C., and van Leeuwen, T. G. (2005) Toward assessment of blood oxygen saturation by spectroscopic optical coherence tomography. *Opt. Lett.* 30(9): 1015–1017.



41. Kagemann, L., Wollstein, G., Wojtkowski, M., Ishikawa, H., Townsend, K. A., Gabriele, M. L., Srinivasan, V. J., Fujimoto, J. G., and Schuman, J. S. (2007) Spectral oximetry assessed with high-speed ultra-high-resolution optical coherence tomography. *J. Biomed. Opt.* 12(4): 041212.
42. Lu, C. W., Lee, C. K., Tsai, M. T., Wang, Y. M., and Yang, C. C. (2008) Measurement of the hemoglobin oxygen saturation level with spectroscopic spectral-domain optical coherence tomography. *Opt. Lett.* 33(5): 416–418.
43. Liu, X., and Kang, J. U. (2010) Depth-resolved blood oxygen saturation assessment using spectroscopic common-path Fourier domain optical coherence tomography. *IEEE Trans. Biomed. Eng.* 57(10): 2572–2575.
44. Robles, F. E., Chowdhury, S., and Wax, A. (2010) Assessing hemoglobin concentration using spectroscopic optical coherence tomography for feasibility of tissue diagnostics. *Biomed. Opt. Express* 1(1): 310–317.
45. Yi, J., and Li, X. (2010) Estimation of oxygen saturation from erythrocytes by high-resolution spectroscopic optical coherence tomography. *Opt. Lett.* 35(12): 2094–2096.
46. Bosschaart, N., Faber, D. J., van Leeuwen, T. G., and Aalders, M. C. (2011) In vivo low-coherence spectroscopic measurements of local hemoglobin absorption spectra in human skin. *J. Biomed. Opt.* 16(10): 100504.
47. Robles, F. E., Wilson, C., Grant, G., and Wax, A. (2011) Molecular imaging true-colour spectroscopic optical coherence tomography. *Nat. Photonics* 5(12): 744–747.
48. Yi, J., Wei, Q., Liu, W., Backman, V., and Zhang, H. F. (2013) Visible-light optical coherence tomography for retinal oximetry. *Opt. Lett.* 38(11): 1796–1798.
49. Yi, J., Chen, S., Backman, V., and Zhang, H. F. (2014) In vivo functional microangiography by visible-light optical coherence tomography. *Biomed. Opt. Express* 5(10): 3603–3612.
50. Chen, S. Y., Yi, J., and Zhang, H. F. (2015) Measuring oxygen saturation in retinal and choroidal circulations in rats using visible light optical coherence tomography angiography. *Biomed. Opt. Express* 6(8): 2840–2853.
51. Chong, S. P., Merkle, C. W., Leahy, C., Radhakrishnan, H., and Srinivasan, V. J. (2015) Quantitative microvascular hemoglobin mapping using visible light spectroscopic Optical Coherence Tomography. *Biomed. Opt. Express* 6(4): 1429–1450.
52. Jaedicke, V., Agaer, S., Robles, F. E., Steinert, M., Jones, D., Goebel, S., Gerhardt, N. C., Welp, H., and Hofmann, M. R. (2013) Comparison of different metrics for analysis and visualization in spectroscopic optical coherence tomography. *Biomed. Opt. Express* 4(12): 2945–2961.
53. Tyo, J. S., Konsolakis, A., Diersen, D. I., and Olsen, R. C. (2003) Principal-components-based display strategy for spectral imagery. *IEEE Trans. Geosci. Remote Sens.* 41(3): 708–718.
54. Adler, D. C., Ko, T. H., Herz, P. R., and Fujimoto, J. G. (2004) Optical coherence tomography contrast enhancement using spectroscopic analysis with spectral autocorrelation. *Opt. Express* 12(22): 5487–5501.
55. Tay, B. C. M., Chow, T. H., Ng, B. K., and Loh, T. K. S. (2012) Dual-window dual-bandwidth spectroscopic optical coherence tomography metric for qualitative scatterer size differentiation in tissues. *IEEE Trans. Biomed. Eng.* 59(9): 2439–2448.
56. Digman, M. A., Caiolfa, V. R., Zama, M., and Gratton, E. (2008) The phasor approach to fluorescence lifetime imaging analysis. *Biophys. J.* 94(2): L14–L16.
57. Fereidouni, F., Bader, A. N., and Gerritsen, H. C. (2012) Spectral phasor analysis allows rapid and reliable unmixing of fluorescence microscopy spectral images. *Opt. Express* 20(12): 12729–12741.
58. Hartigan, J. A., and Wong, M. A. (1979) Algorithm AS 136: A k-means clustering algorithm. *J. R. Soc. Ser. C: Appl. Stat.* 28(1): 100–108.
59. Kohonen, T. (1990) The self-organizing map. *Proc. IEEE* 78(9): 1464–1480.
60. Suykens, J. A., and Vandewalle, J. (1999) Least squares support vector machine classifiers. *Neural Process. Lett.* 9(3): 293–300.
61. Hockel, M., Schlenger, K., Aral, B., Mitze, M., Schaffer, U., and Vaupel, P. (1996) Association between tumor hypoxia and malignant progression in advanced cancer of the uterine cervix. *Cancer Res.* 56(19): 4509–4515.
62. Sebag, J., Delori, F. C., Fekke, G. T., and Weiter, J. J. (1989) Effects of optic atrophy on retinal blood-flow and oxygen-saturation in humans. *Arch. Ophthalmol.* 107(2): 222–226.

63. Hardarson, S. H., and Stefansson, E. (2012) Retinal oxygen saturation is altered in diabetic retinopathy. *Br. J. Ophthalmol.* 96(4): 560–563.
64. Jobsis, F. F. (1977) Noninvasive, infrared monitoring of cerebral and myocardial oxygen sufficiency and circulatory parameters. *Science* 198(4323): 1264–1267.
65. McCully, K. K., and Hamaoka, T. (2000) Near-infrared spectroscopy: What can it tell us about oxygen saturation in skeletal muscle? *Exerc. Sport. Sci. Rev.* 28(3): 123–127.
66. Haacke, E. M., Lai, S., Reichenbach, J. R., Kuppusamy, K., Hoogenraad, F. G., Takeichi, H., and Lin, W. (1997) In vivo measurement of blood oxygen saturation using magnetic resonance imaging: A direct validation of the blood oxygen leveldependent concept in functional brain imaging. *Hum. Brain Mapp.* 5(5): 341–346.
67. Sakadzic, S., Roussakis, E., Yaseen, M. A., Mandeville, E. T., Srinivasan, V. J., Arai, K., Ruvinskaya, S., Devor, A., Lo, E. H., Vinogradov, S. A., and Boas, D. A. (2010) Two-photon high-resolution measurement of partial pressure of oxygen in cerebral vasculature and tissue. *Nat. Methods* 7(9): 755–759.
68. Zhang, H. F., Maslov, K., Stoica, G., and Wang, L. V. (2006) Functional photoacoustic microscopy for high-resolution and noninvasive in vivo imaging. *Nat. Biotechnol.* 24(7): 848–851.
69. Zhang, H. F., Maslov, K., Sivaramakrishnan, M., Stoica, G., and Wang, L. V. (2007) Imaging of hemoglobin oxygen saturation variations in single vessels in vivo using photoacoustic microscopy. *Appl. Phys. Lett.* 90(5): 053901.
70. Prahl, S. (1999) Optical properties spectra. <http://omlc.org/spectra/>.
71. Choi, W., Mohler, K. J., Potsaid, B., Lu, C. D., Liu, J. J., Jayaraman, V., Cable, A. E., Duker, J. S., Huber, R., and Fujimoto, J. G. (2013) Choriocapillaris and choroidal microvasculature imaging with ultrahigh speed OCT angiography. *PLoS One* 8(12): e81499.
72. Matsunaga, D., Yi, J., Puliafito, C. A., and Kashani, A. H. (2014) OCT angiography in healthy human subjects. *Ophthalmic Surg. Lasers Imaging Retina* 45(6): 510–515.
73. Moul, E., Choi, W., Waheed, N. K., Adhi, M., Lee, B., Lu, C. D., Jayaraman, V., Potsaid, B., Rosenfeld, P. J., Duker, J. S., and Fujimoto, J. G. (2014) Ultrahigh-speed swept-source OCT angiography in exudative AMD. *Ophthalmic Surg. Lasers Imaging Retina* 45(6): 496–505.
74. Shah, P. K. (2003) Mechanisms of plaque vulnerability and rupture. *J. Am. Coll. Cardiol.* 41(4 Suppl S): 15S–22S.
75. Kim, J. Y., Lee, M. W., and Yoo, H. (2014) Diagnostic fiber-based optical imaging catheters. *Biomed. Eng. Lett.* 4(3): 239–249.
76. Xu, C., Schmitt, J. M., Carlier, S. G., and Virmani, R. (2008) Characterization of atherosclerosis plaques by measuring both backscattering and attenuation coefficients in optical coherence tomography. *J. Biomed. Opt.* 13(3): 034003–034008.
77. Tearney, G. J., Regar, E., Akasaka, T., Adriaenssens, T., Barlis, P., Bezerra, H. G., Bouma, B., Bruining, N., Cho, J. M., Chowdhary, S., Costa, M. A., de Silva, R., Dijkstra, J., Di Mario, C., Dudek, D., Falk, E., Feldman, M. D., Fitzgerald, P., Garcia-Garcia, H. M., Gonzalo, N., Granada, J. F., Guagliumi, G., Holm, N.R., Honda, Y., Ikeno, F., Kawasaki, M., Kochman, J., Koltowski, L., Kubo, T., Kume, T., Kyono, H., Lam, C. C., Lamouche, G., Lee, D. P., Leon, M. B., Maehara, A., Manfrini, O., Mintz, G. S., Mizuno, K., Morel, M. A., Nadkarni, S., Okura, H., Otake, H., Pietrasik, A., Prati, F., Raber, L., Radu, M. D., Rieber, J., Riga, M., Rollins, A., Rosenberg, M., Sirbu, V., Serruys, P. W., Shimada, K., Shinke, T., Shite, J., Siegel, E., Sonoda, S., Suter, M., Takarada, S., Tanaka, A., Terashima, M., Thim, T., Uemura, S., Ughi, G. J., van Beusekom, H. M., van der Steen, A. F., van Es, G. A., van Soest, G., Virmani, R., Waxman, S., Weissman, N. J., and Weisz, G. (2012) Consensus standards for acquisition, measurement, and reporting of intravascular optical coherence tomography studies: A report from the international working group for intravascular optical coherence tomography standardization and validation. *J. Am. Coll. Cardiol.* 59(12): 1058–1072.
78. Fleming, C. P., Eckert, J., Halpern, E. F., Gardecki, J. A., and Tearney, G. J. (2013) Depth resolved detection of lipid using spectroscopic optical coherence tomography. *Biomed. Opt. Express* 4(8): 1269–1284.
79. Grossman, W., and Baim, D. S. (2006) *Grossman's cardiac catheterization, angiography, and intervention*. Williams & Wilkins, Lippincott, Baltimore, MD.

80. Nam, H. S., Song, J. W., Jang, S. J., Lee, J. J., Oh, W. Y., Kim, J. W., and Yoo, H. (2016) Characterization of lipid-rich plaques using spectroscopic optical coherence tomography. *J. Biomed. Opt.* 21 (7): 075004.
81. Jacques, S. L. (2013) Optical properties of biological tissues: A review. *Phys. Med. Biol.* 58(11): R37–61.
82. Zhao, Y., Maher, J. R., Kim, J., Selim, M. A., Levinson, H., and Wax, A. (2015) Evaluation of burn severity in vivo in a mouse model using spectroscopic optical coherence tomography. *Biomed. Opt. Express* 6(9): 3339–3345.
83. Hong, G., Antaris, A. L., and Dai, H. (2017) Near-infrared fluorophores for biomedical imaging. *Nat. Biomed. Eng.* 1: 0010.
84. Xu, C., Ye, J., Marks, D. L., and Boppart, S. A. (2004) Near-infrared dyes as contrast-enhancing agents for spectroscopic optical coherence tomography. *Opt. Lett.* 29(14): 1647–1649.
85. Kim, C. S., Wilder-Smith, P., Ahn, Y. C., Liaw, L. H., Chen, Z., and Kwon, Y. J. (2009) Enhanced detection of early-stage oral cancer in vivo by optical coherence tomography using multimodal delivery of gold nanoparticles. *J. Biomed. Opt.* 14(3): 034008.
86. Zagaynova, E. V., Shirmanova, M. V., Kirillin, M. Y., Khlebtsov, B. N., Orlova, A. G., Balalaeva, I. V., Sirotkina, M. A., Bugrova, M. L., Agrba, P. D., and Kamensky, V. A. (2008) Contrasting properties of gold nanoparticles for optical coherence tomography: Phantom, in vivo studies and Monte Carlo simulation. *Phys. Med. Biol.* 53(18): 4995–5009.
87. Chen, J., Saeki, F., Wiley, B. J., Cang, H., Cobb, M. J., Li, Z. Y., Au, L., Zhang, H., Kimmey, M. B., Li, X., and Xia, Y. (2005) Gold nanocages: Bioconjugation and their potential use as optical imaging contrast agents. *Nano. Lett.* 5(3): 473–477.
88. Troutman, T. S., Barton, J. K., and Romanowski, M. (2007) Optical coherence tomography with plasmon resonant nanorods of gold. *Opt. Lett.* 32(11): 1438–1440.
89. Cho, E. C., Au, L., Zhang, Q., and Xia, Y. (2010) The effects of size, shape, and surface functional group of gold nanostructures on their adsorption and internalization by cells. *Small* 6(4): 517–522.
90. Cang, H., Sun, T., Li, Z. Y., Chen, J. Y., Wiley, B. J., Xia, Y. N., and Li, X. D. (2005) Gold nanocages as contrast agents for spectroscopic optical coherence tomography. *Opt. Lett.* 30(22): 3048–3050.
91. Oldenburg, A. L., Xu, C. Y., and Boppart, S. A. (2007) Spectroscopic optical coherence tomography and microscopy. *IEEE J. Sel. Top Quantum Electron.* 13(6): 1629–1640.
92. Oldenburg, A. L., Hansen, M. N., Ralston, T. S., Wei, A., and Boppart, S. A. (2009) Imaging gold nanorods in excised human breast carcinoma by spectroscopic optical coherence tomography. *J. Mater. Chem.* 19(35): 6407–6411.
93. Li, Y. L., Seekell, K., Yuan, H. K., Robles, F. E., and Wax, A. (2012) Multispectral nanoparticle contrast agents for true-color spectroscopic optical coherence tomography. *Biomed. Opt. Express* 3(8): 1914–1923.
94. Grant, S. A., Spradling, C. S., Grant, D. N., Fox, D. B., Jimenez, L., Grant, D. A., and Rone, R. J. (2014) Assessment of the biocompatibility and stability of a gold nanoparticle collagen bioscaffold. *J. Biomed. Mater. Res. A* 102(2): 332–339.
95. Shukla, R., Bansal, V., Chaudhary, M., Basu, A., Bhonde, R. R., and Sastry, M. (2005) Biocompatibility of gold nanoparticles and their endocytotic fate inside the cellular compartment: a microscopic overview. *Langmuir* 21(23): 10644–10654.
96. Kumar, V., Abbas, A., Fausto, N., and Aster, J. C. (2014) *Robbins and Cotran pathologic basic of disease*. Elsevier, Atlanta, GA.
97. Graf, R. N., and Wax, A. (2005) Nuclear morphology measurements using Fourier domain low coherence interferometry. *Opt. Express* 13(12): 4693–4698.
98. Graf, R. N., Robles, F. E., Chen, X. X., and Wax, A. (2009) Detecting precancerous lesions in the hamster cheek pouch using spectroscopic white-light optical coherence tomography to assess nuclear morphology via spectral oscillations. *J. Biomed. Opt.* 14(6).
99. Robles, F. E., Zhu, Y. Z., Lee, J., Sharma, S., and Wax, A. (2010) Detection of early colorectal cancer development in the azoxymethane rat carcinogenesis model with Fourier domain low coherence interferometry. *Biomed. Opt. Express* 1(2): 736–745.